

PROCEEDINGS OF SPIE

SPIDigitalLibrary.org/conference-proceedings-of-spie

A multi-resolution analysis-based approach to accelerate data acquisition for near-field MIMO millimeter-wave imaging

Molaei, Amir Masoud, Hu, Shaoqing, Fusco, Vincent, Yurduseven, Okan

Amir Masoud Molaei, Shaoqing Hu, Vincent Fusco, Okan Yurduseven, "A multi-resolution analysis-based approach to accelerate data acquisition for near-field MIMO millimeter-wave imaging," Proc. SPIE 12111, Passive and Active Millimeter-Wave Imaging XXV, 121110J (3 June 2022); doi: 10.1117/12.2622826

SPIE.

Event: SPIE Defense + Commercial Sensing, 2022, Orlando, Florida, United States

A multi-resolution analysis-based approach to accelerate data acquisition for near-field MIMO millimeter-wave imaging

Amir Masoud Molaei^{*a}, Shaoqing Hu^b, Vincent Fusco^a, Okan Yurduseven^a

^aInstitute of Electronics, Communications and Information Technology (ECIT), Queen's University Belfast, Queen's Road, Belfast, U.K. BT3 9DT; ^bCollege of Engineering, Design and Physical Sciences, Brunel University London, Kingston Lane, Uxbridge, U.K. UB8 3PH

ABSTRACT

An approach to designing multiple waveforms in a multiple-input multiple-output (MIMO) system is presented so that the full capacity of the transmitting and receiving antennas can be utilized at the same time. On the transmitter-side, the antenna elements are classified into different groups according to their specific signal. On the receive-side, we use a multi-resolution analysis to retrieve the signals of each channel. Due to the superior characteristics of the FMCW signal, especially in terms of sampling, in the proposed approach, an FMCW radar is considered. To adapt the introduced system to multistatic near-field imaging, we use more accurate models than the effective phase center principle. This contributes to the successful reconstruction of the scene image by efficient Fourier-based image reconstruction methods. The performance of the proposed approach is confirmed by numerical simulations.

Keywords: mm-wave imaging, MIMO, multi-resolution analysis, near-field

1. INTRODUCTION

In recent decades, wireless communication systems have experienced rapid growth in the use of multiple-input multiple-output (MIMO) technology in applications such as mobile radio networks, the Internet of things (IoT), and military and civilian radars [1, 2]. Advantages such as higher data rate, reduced signal distortion and higher accuracy obtained through the use of multiple transmitter (Tx) and receiver (Rx) combinations, have been among the reasons for the increasing development of this technology compared to conventional technologies such as single-input single-output (SISO) and single-input multiple-output (SIMO) [3]. However, MIMO systems usually require higher levels of design and signal processing in the Tx and Rx sections. An important challenge in using MIMO systems is the need to generate optimal signals that are orthogonal to each other (so-called waveform diversity) [4]; in other words, the transmitted waveforms must be designed and optimized in such a way that all pairs of individual Tx-Rx signals can be separated from the composite received signal at the Rx. Also, accurate retrieval of each pair of signals requires some efficient processing on the Rx.

One of the popular methods for implementing waveform diversity is the use of various multiple access techniques [5]. The time-division technique [6] is known as the simplest method for obtaining orthogonal signals. The basis of this technique is to transmit signals of each Tx at non-overlapping time intervals with other Tx's. In other words, at each time slot, only one Tx transmits and the Rx's receive only one signal corresponding to that single Tx. It is clear that such a mechanism, despite its simplicity, may significantly increase the overall transmitting time. The frequency-division technique [7] is another common method in which the transmitted signals have no frequency overlap; in other words, each signal occupies a specific bandwidth in the spectral domain. Although the signals of all Tx's can be transmitted simultaneously using the frequency-division technique, such a mechanism typically requires a very wide overall frequency bandwidth. Such an extended bandwidth may be wider than what the received signal can be sampled by using present-day analog-to-digital converters (ADCs) and digital-to-analog converters. In addition, if the total bandwidth in the time-division and frequency-division techniques are considered the same, then the latter leads to a worse range resolution because each Tx uses only part of the total bandwidth. In the code-division technique [8], all Tx's transmit signals with the same central frequency, and bandwidth is shared between the Tx's. Therefore, this technique does not require increasing the sampling rate. However, as the number of Tx's increases, in addition to complicating the system, the overall quality of services decreases [9].

^{*}a.molaei@qub.ac.uk; fax 44 28 9097 1702; pure.qub.ac.uk/en/persons/amir-masoud-molaei

Millimeter-wave (mm-wave) radars are a special class of radar technology that use short wavelength electromagnetic waves [10]. These radars are used today in various applications such as advanced driving assistant systems, building automation, health monitoring and security scanning [11]. Continuous-wave (CW) radars have less hardware complexity than pulse radars. However, most orthogonal signals generation techniques have been developed for pulse radars, which are not necessarily applicable to CW radars (including frequency-modulated CW (FMCW) radars). FMCW radars are very popular in automotive and industrial applications due to some of their unique specifications. An important advantage of the FMCW signal is that the beat signal bandwidth is much less than the instantaneous bandwidth. This, in particular in terms of sampling, leads to much-desired simplification of the ADC acquisition.

Recently in [4], an efficient mechanism for waveform diversity in a MIMO structure is proposed. The Tx's are first classified into several groups, and the same carrier frequency is assigned to the corresponding signals of the Tx's in each group. The carrier frequency of each group has a small offset compared to those other groups. The waveforms of each group are then encoded. Due to the waveform diversity feature, all Tx's will be able to submit simultaneously. On the Rx-side, the received signals must be decoded. However, it is not possible to perform this operation without retrieving the content corresponding to the groups. Applying a multi-resolution analysis approach can be an effective solution for retrieving all pairs. In this paper, step-by-step implementations on the Rx-side to retrieve all pairs of Tx-Rx signals, along with some analysis of the performance of two multi-resolution analysis methods called variational mode decomposition (VMD) and successive VMD (SVMD) [12, 13], are addressed. Moreover, the mentioned approach is specifically examined in the case of a near-field (NF) MIMO imaging system, and in addition to the analysis of the processed signals, the results are also presented in the form of reconstructed images.

The rest of this paper is organized as follows: in Section 2, the system model is presented; in Section 3, the design model on the Tx-side and the processing procedures on the Rx-side are described; Section 4 is devoted to the presentation of results and analyzes; Section 5 provides a brief conclusion.

2. SYSTEM MODEL

Consider an FMCW signal whose instantaneous frequency changes linearly with time as follows:

$$s_o(t) = e^{j2\pi(f_0 t + 0.5\beta t^2)}, \quad 0 < t < T_p, \quad (1)$$

where f_0 represents the carrier frequency at $t = 0$, and j is the imaginary unit. β and T_p are the chirp rate and chirp pulse duration, respectively, and determine the signal bandwidth $B = \beta T_p$. $s_o(t)$ constitutes the main nature (not the final form) of the Tx-side signal for the mm-wave radar in this paper. Before transmitting, some changes in frequency and phase of $s_o(t)$ are applied, the details of which are given in Section 3.1. Figure 1 shows the general structure of the imaging system considered in this paper. It is assumed that two uniform linear arrays (ULAs), as Tx and Rx, with a horizontal distance d_o (along the x-axis), located parallel to the y-axis (vertically), are used in a MIMO structure and perform the task of electronic scanning. The number of elements in these arrays and the inter-element distances are denoted by N_t , N_r , d_t and d_r , respectively. In order to form a two-dimensional (2D) aperture, and thus obtain scene information in both the x- and y-directions, a 1D mechanical scanning is also performed horizontally by moving the arrays with fixed sampling steps d_x (a total of N_x steps). Based on the effective phase center principle, under the far-field (FF) assumption, a multistatic array topology with $N_t + N_r$ physical antennas can be considered as a monostatic virtual array with $N_t N_r$ elements (equal to the number of all channels) [14]. It can easily be proved that if d_t is considered equal to $N_r d_r$, a virtual ULA is provided with an inter-element spacing of $d_r/2$.

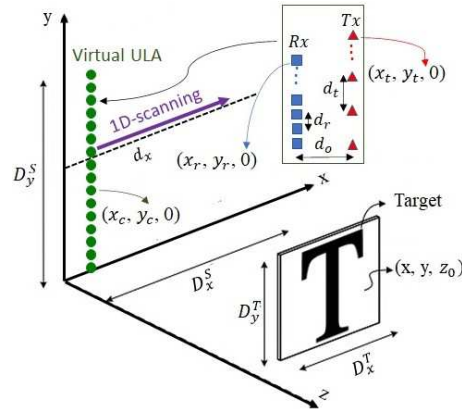


Figure 1. The general structure of the imaging system.

3. DESIGN AND PROCESSING APPROACH

3.1 Tx-side

According to the designs done in [4], on the Tx-side, first, N_T Tx antennas are divided into G non-overlapping groups so that $\sum_{g=0}^{G-1} P_g$, where P_g represents the number of Tx antennas in the g^{th} group, and $g=0,1,\dots,G-1$ and $P_g \in \{2^n \mid n=0,1,2,\dots\}$. This division is shown visually in Figure 2. In this figure, for simplicity, it is assumed that the adjacent antennas are in the same groups, which is not necessary. The same carrier frequency is assigned to all chirp signals in the g^{th} group (i.e. $s_{g,p}(t)$, where $p=1,2,\dots,P_g$). The carrier frequency of each group has a small offset f_Δ compared to the previous group, so that $f_\Delta \ll f_0$. Finally, before transmitting, the signals within the g^{th} group are encoded by assigning a binary phase in a time block of length $P_g T_p$ [4]. Figure 3, for example, shows how the signals corresponding to group 1 are encoded for a sequence of four distinct codes, denoted by C_1, C_2, C_3 and C_4 , assuming that group 1 contains four Tx antennas. The mathematical form of the transmitted signals can be written as follows (see Figure 2):

$$s_{g,p}(t) = e^{j(2\pi((f_0 - g f_\Delta)t + 0.5\beta t^2) - \phi_{g,p})}, \quad 0 < t < P_g T_p, \quad (2)$$

where $\phi_{g,p}$ represents the binary phase encoded by Walsh-Hadamard codes [15]. Figure 4 shows a summary of the steps mentioned above in the form of a block diagram.

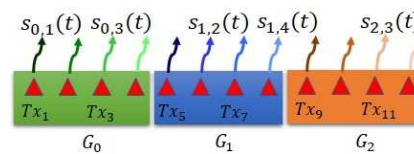


Figure 2. Mechanism of grouping Tx antennas and assigning signals to them, assuming 12 Tx antennas and 3 groups (each containing 4 antennas).

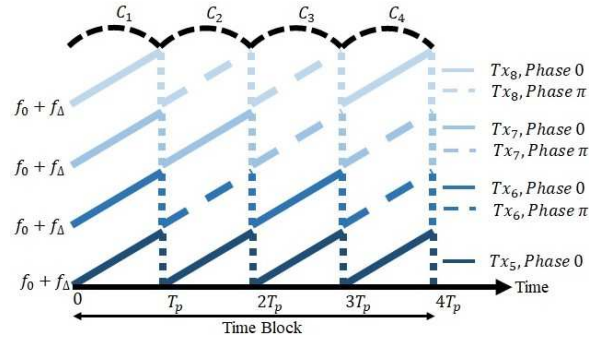


Figure 3. Encoded chirp sequences in group 1 assuming four Tx antennas.

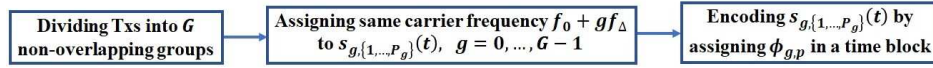


Figure 4. Block diagram of design steps on the Tx-side.

3.2 Rx-side

In case of simultaneous transmission by all Tx antennas, the combined signal received by the i' -th Rx antenna can be mathematically written as follows:

$$s_{i'}(t) = \sum_{g=0}^{G-1} \sum_{p=1}^{P_g} s_{i',g,p}(t) + n_{i'}(t), \quad (3)$$

where $n_{i'}(t)$ represents noise, and $s_{i',g,p}(t)$ can be written in simplified form to the following form [4]:

$$s_{i',g,p}(t) = l e^{j[2\pi(f_0\tau_{i',g,p} + (\beta\tau_{i',g,p} + gf_\Delta)t) + \phi_{g,p}]}, \quad (4)$$

where $\beta\tau_{i',g,p}$ is known as the *beat frequency*, whose sum with gf_Δ forms the *desired frequency*. In (4), l and τ represent the combination of target reflectivity σ and the round-trip amplitude decay off the target, and the round-trip delay, respectively, which are calculated as follows:

$$l = \frac{\sigma}{R_i R_r}, \quad \tau = \frac{R_i + R_r}{c}, \quad R_i = \sqrt{(x - x_i)^2 + (y - y_i)^2 + z_0^2}, \quad R_r = \sqrt{(x_r - x)^2 + (y_r - y)^2 + z_0^2}, \quad (5)$$

where c is the speed of light.

The challenge here is that the raw data collected by the Rx's cannot be processed directly for the image reconstruction process; because the individual data of each Tx-Rx pair are integrated into the combined signal. This is where applying a multi-resolution analysis can help us to separate the composite signals belonging to each group as well as retrieve the original content of the data. Our focus in this paper is on two efficient VMD and SVMD methods [16]. The VMD is able to decompose a multicomponent signal $x(t)$ into N_b band-limited sub-signals u_n called intrinsic mode functions (IMFs) [17]:

$$x(t) = \sum_{n=1}^{N_b} u_n(t). \quad (6)$$

VMD can be written as a constrained variational problem as follows [18]:

$$\min_{\{u_n\}, \{f_n\}} \left\{ \sum_{n=1}^{N_b} \|dB(t)/dt\|_2^2 \right\}, \quad s.t. \sum_{n=1}^{N_b} u_n = x, \quad (7)$$

where f_n is the central frequency around which each mode is compacted, $B(t)$ is the base frequency spectrum [19], and $\|\cdot\|_2^2$ denotes the squared L^2 -norm. Equation (7) can be solved by introducing a quadratic penalty and Lagrangian multipliers [18]. In the case of SVM, decomposition is performed by successively applying variational mode extraction to the signal and adding some constraints to avoid convergence to the previous extracted modes. This procedure continues until all modes are extracted or the reconstruction error is less than a threshold. It can be mathematically assumed that $x(t)$ is decomposed into two signals $u_n(t)$ and $x_r(t)$ [13]:

$$x(t) = u_n(t) + x_r(t), \quad N \in [1, n], \quad (8)$$

where the residual signal $x_r(t)$ is the input signal excluding $u_n(t)$ and consists of two components: the sum of the previously obtained modes and the unprocessed part of the signal ($x_u(t)$) [13]:

$$x_r(t) = \sum_{n=1}^{N-1} u_n(t) + x_u(t). \quad (9)$$

Details of implementing SVM can be found in [13].

After recovering the composite signals of each group by a multi-resolution analysis, the composite signals are decoded to retrieve the signals corresponding to all pairs of Tx-Rx. Data decoding is done according to the type of encoding used on the Tx-side. In addition, after decoding, it is necessary to return the signal frequency content from the desired frequency to the beat frequency. This can be done simply by multiplying the received complex signals in the g^{th} group by $e^{-j2\pi g \Delta t}$. Now, the received beat signal can be rewritten in the wavenumber domain as follows:

$$s(x_T, y_T, x_R, y_R, k) = \sigma \frac{e^{jk(R_t + R_r)}}{R_t R_r}, \quad (10)$$

where $k = 2\pi f/c$ represents the wavenumber corresponding to the instantaneous frequency $f = f_0 + \beta t$. Accordingly, what we will have as the input of the image reconstruction algorithm is a $N_t \times N_r \times N_x \times N_s$ data (which we call $\hat{\mathcal{S}}$) whose complex values are the measurements captured by each Tx-Rx pair, in each spatial and temporal sampling, where N_s denotes the number of sampled points in duration T_p . A summary of the main processing steps on the Rx-side is given in Figure 5.

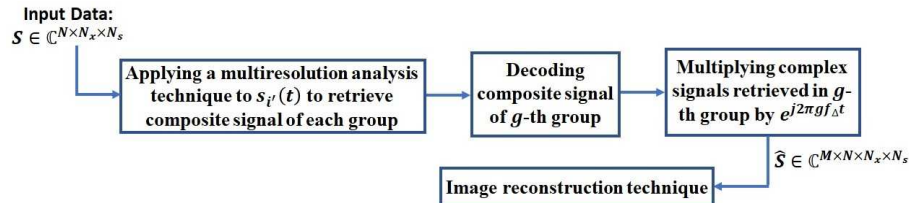


Figure 5. Summary of the main processing steps on the Rx-side.

4. SIMULATION RESULTS

In this section, some of the simulation results are given. For the studies presented in this section, all computations were done on MATLAB R2020b of 64-bit Windows 10 operating system with 12GB of random-access memory and a Core-i7 central processing unit at 2.7GHz. The conventional FFT-IFFT method is used to reconstruct the images [14]. In order for this method to be effective in the NF, a multistatic-to-monostatic conversion [20] must be used as preprocessing. See [21] for more details. The values of the simulation parameters are given in Table 1, where λ is the wavelength at the center frequency of 79GHz. According to the aperture size and operating frequency presented in Table 1, targets in the range of approximately less than 39m are considered to be located in the NF region [22].

The outputs of the Tx-Rx pairs recovery steps, for example for Rx_{12} at the scanning center point, for a point scatterer in the center of the target area are given below. Figure 6 shows the real and imaginary parts of the combined received signal. Figure 7 shows the real part of the composite signals retrieved in each group by applying the VMD method. As can be seen, despite the fact that the signals are noisy, the recovered signals in all respects of amplitude, frequency and phase, are in good agreement with the original (true) signals. Figure 8 shows the outputs corresponding to Figure 7 when the SVMD method is used instead of the VMD method. It can be clearly seen that the composite signal of group 1 has not been retrieved properly. Also, the retrieved signals of other groups do not have a perfect match with the original signals. To study this more closely, let us take a look at the spectrum of signals (Figure 9). As can be seen, the frequency separation of the modes by the SVMD method is not as good as by the VMD method. In particular, the signal corresponding to group 0 contains more than one frequency component. One reason for this may be the sensitivity of the SVMD method to the frequency distance of the modes. Our experiments have shown that increasing f_{Δ} can be a way to improve the performance of the SVMD method in our case. For example, when we increased f_{Δ} from 95kHz to 200kHz, the outputs of the SVMD method were close to those of the VMD method (see Figure 10). However, it is not desirable to increase the frequency offset f_{Δ} too much, because the closer f_{Δ} is to the sampling frequency, the lower the accuracy of signal retrieval. It should be noted that the average computational time for the decomposition of the modes in Figures 7 and 8 is 0.12Sec and 0.71Sec, respectively. However, the analyzes in [13] show that when the number of modes increases significantly, the SVMD method has a considerable computational advantage over the VMD method. Another advantage of the SVMD method is that, unlike the VMD method, it does not need to know the number of modes. Of course, it should be noted that in our case, the number of modes is equal to the number of groups that are considered in the Tx-side design and the receiver is aware of it. Overall, due to the greater reliability of the VMD method in our example, the continuation of the results is based on the VMD outputs. The next step, after recovering the composite signal of each group, is to decode them so that the signals transmitted from all Tx's can be accessed separately. The results of this step are shown in Figure 11. Finally, before reconstructing the image, the retrieved signals corresponding to the Tx's must be returned from the desired frequency to the beat frequency. Here, just as an example, the outputs of the sixth and ninth Tx's (belonging to groups 1 and 2, respectively) are shown in Figure 12. By performing the above operation for all Rx's and for all spatial sampling points, \hat{S} is obtained. As mentioned in Section 3.2, that is the input to the image reconstruction algorithm. The reconstructed image is shown in Figure 13.

Table 1. Values of simulation parameters.

Parameter	N_t	N_r	d_t	d_r	d_o	z_0	D_x^s	D_y^s	D_x^T	D_y^T
Value	12	24	12λ	$\lambda/2$	4mm	300mm	272mm	272mm	75mm	75mm

Parameter	N_x	f_0	B	β	N_s	f_{Δ}	G	P_0	P_1	P_2	SNR
Value	151	77GHz	4GHz	80 MHz/us	256	95kHz	3	4	4	4	15dB

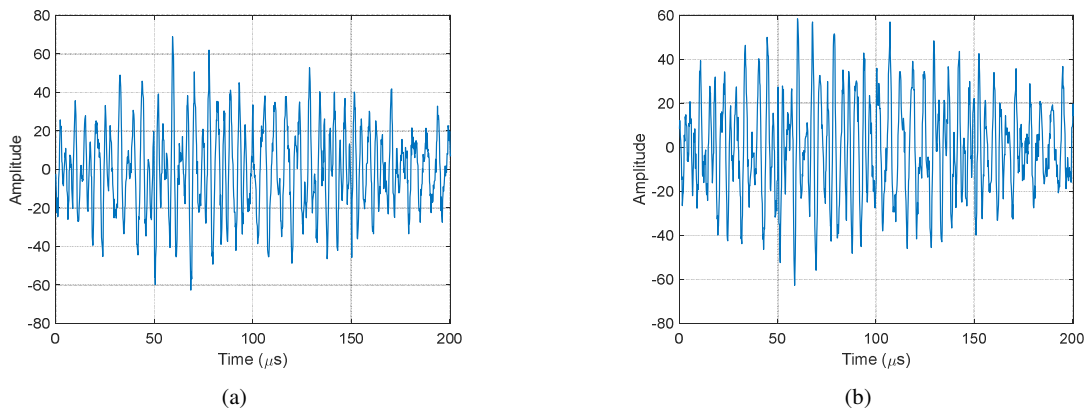


Figure 6. Received combined signal; (a) real part, (b) imaginary part.

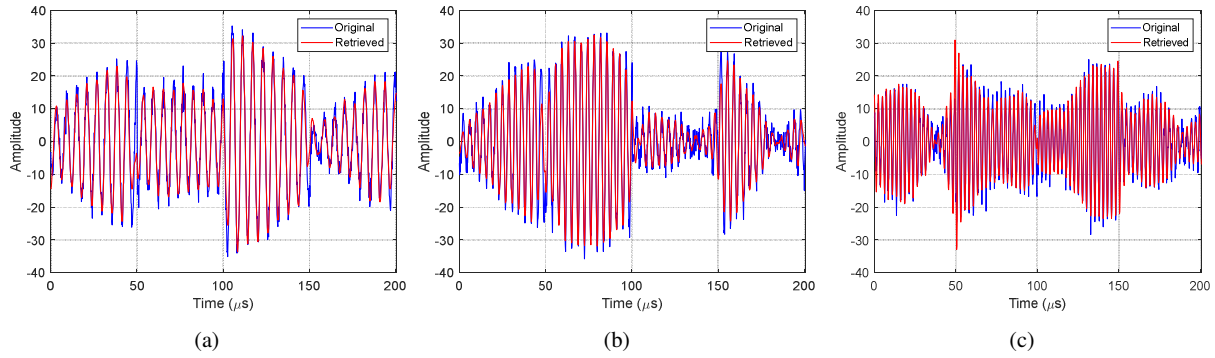


Figure 7. The real part of composite signals retrieved by applying the VMD method; (a) group 0, (b) group 1, (c) group 2.

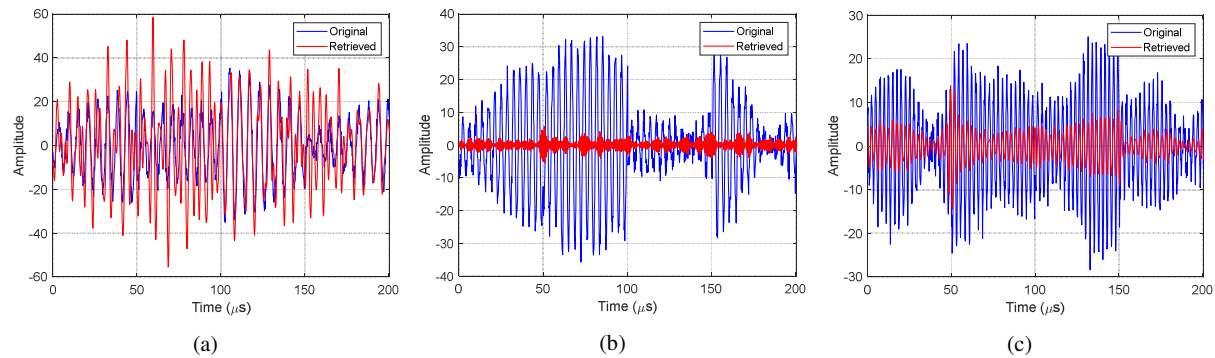


Figure 8. The real part of composite signals retrieved by applying the SVMD method; (a) group 0, (b) group 1, (c) group 2.

We also applied the presented mechanism to image a T-shaped target. In this example, N_x and SNR are assumed to be 288 and 14dB, respectively. The other parameters are similar to the values in Table 1. The final result (reconstructed image) is given in Figure 14. As can be seen, the presented mechanism for a distributed target also worked well. Note that the image quality in the horizontal direction (with mechanical scanning) is better than in the vertical direction (with electronic scanning). The reason for this is the approximations imposed on the data processed by the image reconstruction algorithm by applying multistatic-to-monostatic conversion in the vertical direction. This problem can be improved by increasing the density of the antennas.

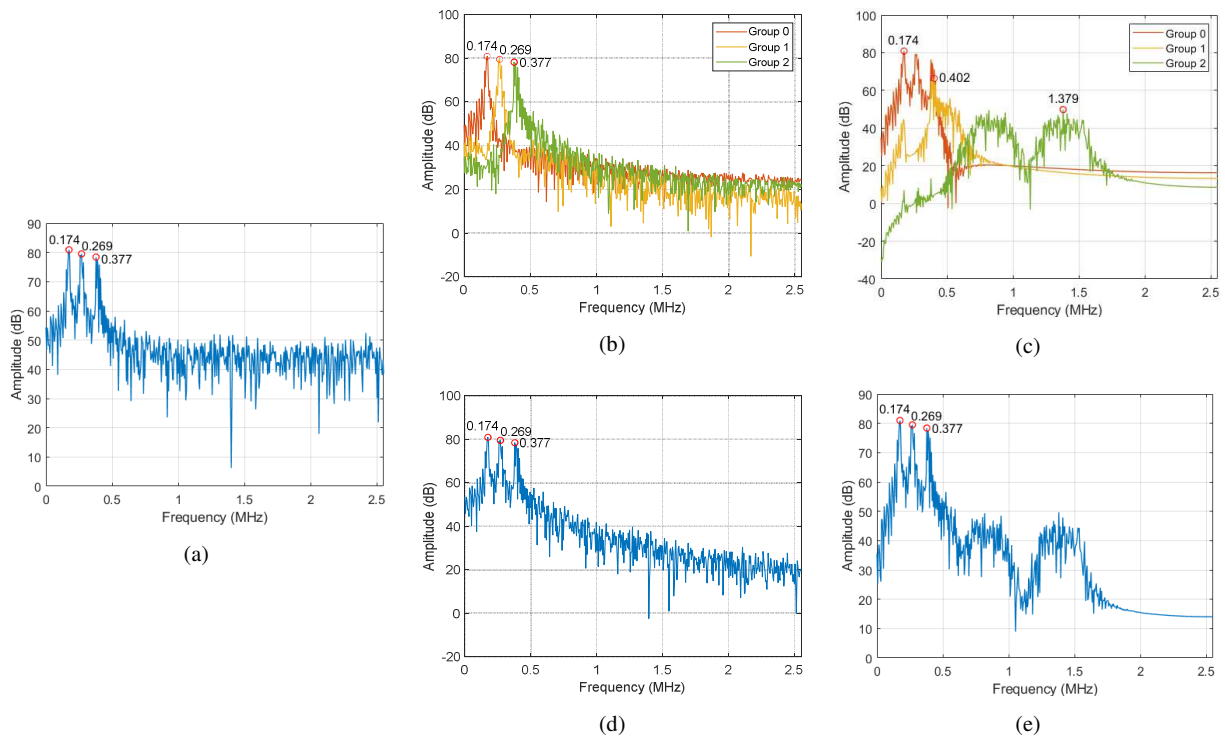


Figure 9. Comparison of the spectral behavior of signals; (a) received combined signal spectrum, (b) corresponding spectra of the composite signals retrieved in each group by VMD method, (c) corresponding spectra of the composite signals retrieved in each group by SVMd method, (d) spectrum obtained by combining modes separated by VMD method, (e) spectrum obtained by combining modes separated by SVMd method.

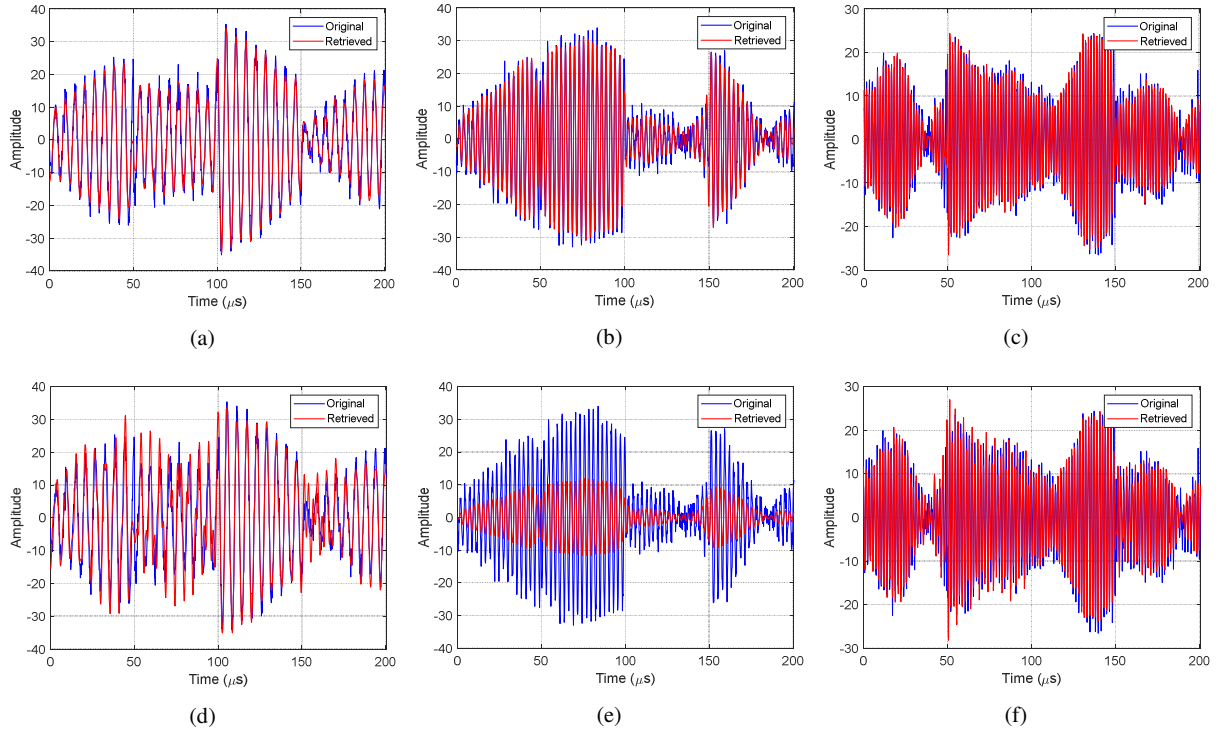


Figure 10. The real part of the retrieved composite signals when $f_{\Delta} = 200\text{KHz}$; (a) VMD method, group 0, (b) VMD method, group 1, (c) VMD method, group 2, (d) SVMD method, group 0, (e) SVMD method, group 1, (f) SVMD method, group 2.

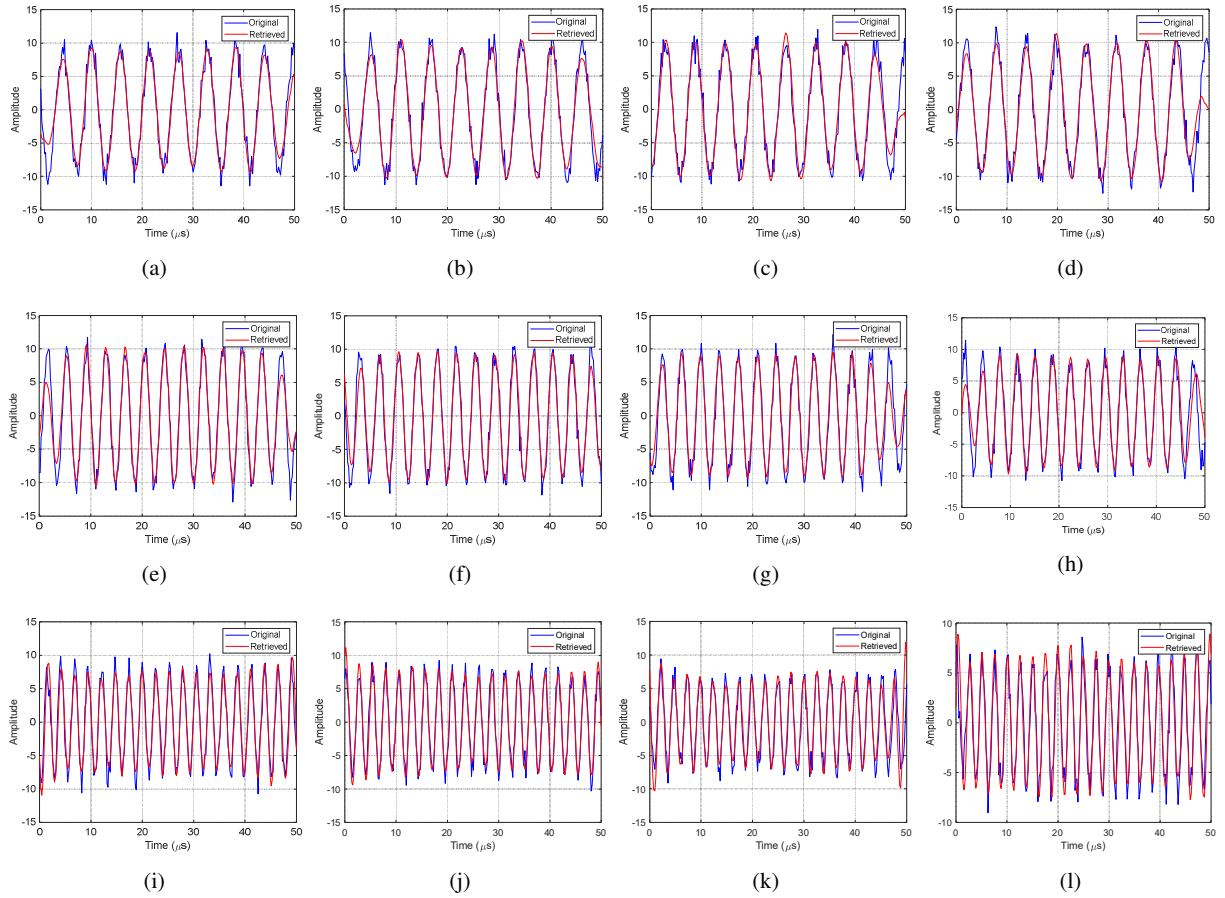


Figure 11. The real part of the retrieved signals corresponding to 12 TxS; (a) Tx_1 , (b) Tx_2 , (c) Tx_3 , (d) Tx_4 , (e) Tx_5 , (f) Tx_6 , (g) Tx_7 , (h) Tx_8 , (i) Tx_9 , (j) Tx_{10} , (k) Tx_{11} , (l) Tx_{12} .

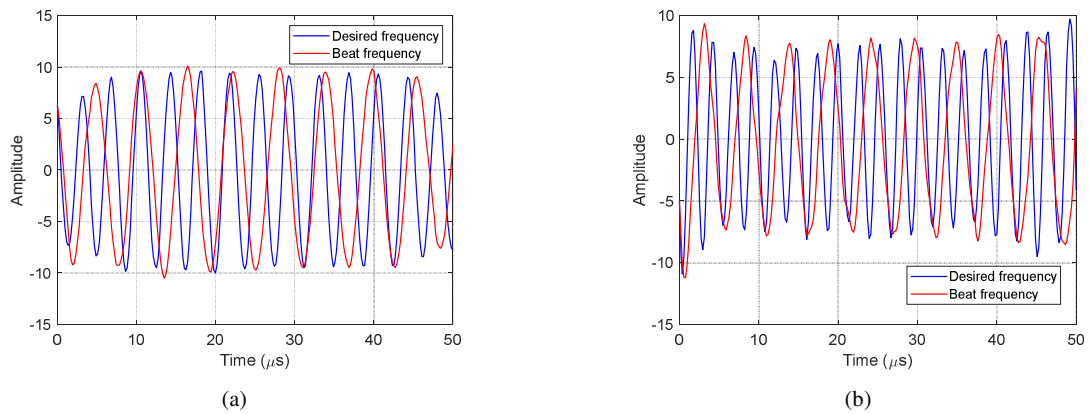


Figure 12. Returning from the desired frequency to the beat frequency; (a) Tx_6 , (b) Tx_9 .

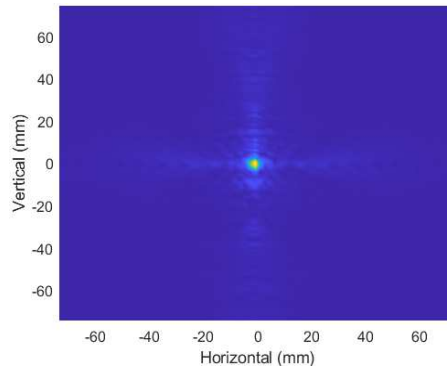


Figure 13. Reconstructed image of a point scatterer.

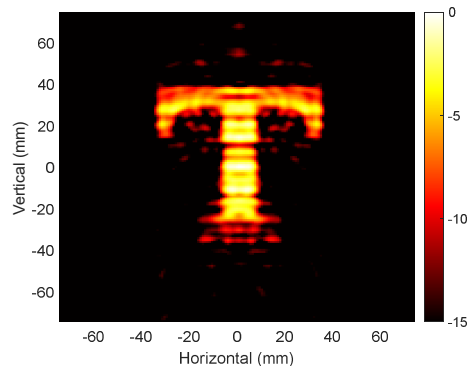


Figure 14. Reconstructed image of a T-shaped target. The values listed on the side of the colorbar are in decibels.

5. CONCLUSION

In this paper, the effectiveness of multi-resolution analysis for the separation of individual Tx-Rx pairs in a NF MIMO imaging scenario with a specific design of the transmitted waveforms was studied. The output of each processing step was shown and discussed. Some comparisons were made between the performance of VMD and SVMD methods. The discussed mechanism can bring significant advantages for data acquisition in MIMO radar systems as all Tx's can transmit simultaneously, suggesting that the data acquisition rate may be significantly improved.

ACKNOWLEDGMENT

This work was funded by the Leverhulme Trust under Research Leadership Award RL-2019-019.

REFERENCES

- [1] S. Singh, B. S. Singla, M. Sharma, S. Goyal, and A. Sabo, "Comprehensive Study on Internet of Things (IoT) and Design Considerations of Various Microstrip Patch Antennas for IoT Applications," in *Mobile Radio Communications and 5G Networks*: Springer, 2021, pp. 19-30.
- [2] F. Gini, "Grand challenges in radar signal processing," *Frontiers in Signal Processing*, vol. 1, p. 1, 2021.
- [3] C. Fager, T. Eriksson, F. Barradas, K. Hausmair, T. Cunha, and J. C. Pedro, "Linearity and efficiency in 5G transmitters: New techniques for analyzing efficiency, linearity, and linearization in a 5G active antenna transmitter context," *IEEE Microwave Magazine*, vol. 20, no. 5, pp. 35-49, 2019.

- [4] A. M. Molaei, O. Yurduseven, and V. Fusco, "An efficient waveform diversity based on variational mode decomposition of coded beat-frequency shifted signals algorithm for multiple-input multiple-output millimetre-wave imaging," *IET Radar, Sonar & Navigation*, vol. 15, no. 10, pp. 1266-1280, 2021.
- [5] H. Mathur and T. Deepa, "A survey on advanced multiple access techniques for 5G and beyond wireless communications," *Wireless Personal Communications*, vol. 118, no. 2, pp. 1775-1792, 2021.
- [6] L. L. Monte, B. Himed, T. Corigliano, and C. J. Baker, "Performance analysis of time division and code division waveforms in co-located MIMO," in *2015 IEEE Radar Conference (RadarCon)*, 2015: IEEE, pp. 0794-0798.
- [7] N. Michailow and G. Fettweis, "Low peak-to-average power ratio for next generation cellular systems with generalized frequency division multiplexing," in *2013 International Symposium on Intelligent Signal Processing and Communication Systems*, 2013: IEEE, pp. 651-655.
- [8] X. Chen, Z. Feng, Z. Wei, P. Zhang, and X. Yuan, "Code-division OFDM joint communication and sensing system for 6G machine-type communication," *IEEE Internet of Things Journal*, vol. 8, no. 15, pp. 12093-12105, 2021.
- [9] Y. Yifei and Z. Longming, "Application scenarios and enabling technologies of 5G," *China Communications*, vol. 11, no. 11, pp. 69-79, 2014.
- [10] P. Verma, V. S. Shakya, D. Sharma, U. Chauhan, and A. Gaur, "MM-Wave Radar Application for Autonomous Vehicles," in *2020 2nd International Conference on Advances in Computing, Communication Control and Networking (ICACCCN)*, 2020: IEEE, pp. 556-559.
- [11] M. Mercuri *et al.*, "2-D localization, angular separation and vital signs monitoring using a SISO FMCW radar for smart long-term health monitoring environments," *IEEE Internet of Things Journal*, vol. 8, no. 14, pp. 11065-11077, 2021.
- [12] Y. Miao, M. Zhao, and J. Lin, "Identification of mechanical compound-fault based on the improved parameter-adaptive variational mode decomposition," *ISA transactions*, vol. 84, pp. 82-95, 2019.
- [13] M. Nazari and S. M. Sakhaei, "Successive variational mode decomposition," *Signal Processing*, vol. 174, p. 107610, 2020.
- [14] A. M. Molaei, S. Hu, V. Skouroliakou, V. Fusco, X. Chen, and O. Yurduseven, "Fast processing approach for near-field terahertz imaging with linear sparse periodic array," 2022.
- [15] C. M. Gómez-Sarabia, L. M. Ledesma-Carrillo, V. H. Espinoza-Godínez, A. Mejía-Arredondo, and J. Ojeda-Castañeda, "Noncoherent binary phase coding: Sequential dual channels," *Optics Communications*, vol. 508, p. 127707, 2022.
- [16] G. Li, C. Zheng, and H. Yang, "Carbon price combination prediction model based on improved variational mode decomposition," *Energy Reports*, vol. 8, pp. 1644-1664, 2022.
- [17] C. Dora and P. K. Biswal, "Correlation-based ECG artifact correction from single channel EEG using modified variational mode decomposition," *Computer Methods and Programs in Biomedicine*, vol. 183, p. 105092, 2020.
- [18] S. Liu, R. Zhao, K. Yu, B. Zheng, and B. Liao, "Output-only modal identification based on the variational mode decomposition (VMD) framework," *Journal of Sound and Vibration*, vol. 522, p. 116668, 2022.
- [19] A. Dibaj, R. Hassannejad, M. M. Etefagh, and M. B. Ehghaghi, "Incipient fault diagnosis of bearings based on parameter-optimized VMD and envelope spectrum weighted kurtosis index with a new sensitivity assessment threshold," *ISA transactions*, vol. 114, pp. 413-433, 2021.
- [20] A. M. Molaei, S. Hu, V. Skouroliakou, V. Fusco, X. Chen, and O. Yurduseven, "Fourier Compatible Near-Field Multiple-Input Multiple-Output Terahertz Imaging With Sparse Non-Uniform Apertures," *IEEE Access*, vol. 9, pp. 157278-157294, 2021.
- [21] V. Skouroliakou, A. M. Molaei, V. Fusco, and O. Yurduseven, "Fourier-Based Radar Processing for Multistatic Millimetre-Wave Imaging with Sparse Apertures," in *European Conference on Antennas and Propagation*, 2021.
- [22] A. M. Molaei, P. del Hougne, V. Fusco, and O. Yurduseven, "Efficient Joint Estimation of DOA, Range and Reflectivity in Near-Field by Using Mixed-Order Statistics and a Symmetric MIMO Array," *IEEE Transactions on Vehicular Technology*, 2021.